Electronic Supporting Information

3D multistage information encryption platform with self-erasure function based on the synergistically shape-deformable and AIE fluorescence-tunable hydrogel

Caixia Yang[abc], Hangxiang Xiao[c], Li Tang[a], Zichen Luo[c], Ying Luo[c], Ningbo Zhou[cd], Enxiang Liang*[cd], Guoxiang Wang*[cd] and Jianxin Tang*[a]

[a]Hunan Key Laboratory of Biomedical Nanomaterials and Devices, College of Life Sciences and Chemistry, Hunan University of Technology, Zhuzhou, 412007, PR China.

[b]College of Packaging and Material Engineering, Hunan University of Technology, Zhuzhou 412007, PR China

[c]College of Chemistry and Chemical Engineering, Hunan Institute of Science and Technology Yueyang, Hunan Province 414006, PR China.

[d]Key Laboratory of Hunan Province for Advanced Carbon-based Functional Materials, School of Chemistry and Chemical Engineering, Hunan Institute of Science and Technology, Yueyang, 414006, PR China

Email: exliang@hnist.edu.cn, wanggxwzl@163.com, jxtang0733@163.com

Materials

Trityl chloride (97%), benzophenone (99.5%), zinc powder (99.9%) fuming nitric acid, Raney Ni, 2-Hydroxy-4′-(2-hydroxyethoxy)-2-methylpropiophenone (I2959) and tetrahydrofuran (THF) were obtained from Aladdin Shanghai Reagent Co.were obtained from Adamas Reagent Co., Ltd (Shanghai, China). Poly(sodium p-styrenesulfonate) was purchased from Sigma Company (China) with an Mw of 70 000 daltons. Acetic acid (glacial), dichloromethane and ethyl acetate and HCHO (37%) were obtained from Tansoole (Shanghai, China). THF was purified by distillation from sodium benzophenone under nitrogen immediately prior to us. Acrylic acid (AA, stabilised with MEHQ) and acryloyl chloride were obtained from TCL (Shanghai, China). N,N-dimethylacrylamide (DMA) and N, N′-methylenebis(acrylamide) (BIS) were purchased from Adamas Reagent Co., Ltd (Shanghai, China). Silica nanoparticle (SN) with concentrations of 50 wt% at pH 9, SiO_2/Na_2O ratios of 200-250, and radii of about 15 nm was obtained from Sigma-Aldrich (Shanghai, China). 2, 2′-Azobisisobutyronitrile (AIBN) (Sigma, 98%) was recrystallised from ethanol. Potassium persulphate (KPS) and N,N,N′,N′-tetramethylethylenediamine (TEMED) used as redox initiators were obtained from Adamas Reagent Co., Ltd (Shanghai, China). All chemicals were used without purification unless otherwise noted.

Methods

NMR spectroscopy. ^{1}H NMR and ^{13}C NMR spectra were recorded on a 400 MHz Bruker spectrometer.

Mass spectroscopy. Mass spectral data were measured with XEVO G2-S QTOF (ESI) (Waters, USA).

UV spectra. UV spectra were measured on a Shimadzu Corporation UV-2600 spectrophotometer. Samples (0.2 mM) were placed in a 10 mm quartz cell.

Fluorescence spectroscopy. The fluorescence spectra were recorded on a Perkin-Elmer LS 55 spectrofluorometer with a Xenon discharge lamp excitation. Samples (0.2 mM) for absorption and emission measurements were carried out in 1 cm × 1 cm quartz cuvettes. And all tests were carried out at room temperature if not mentioned. Regarding the parameter setting of the test fluorescence intensity, the scan rate was 1200 nm/min. The EX slit and EM slit were 5 nm. The PMT Voltage was 400 V

Fluorescence Lifetime Measurements. Fluorescence lifetime was measured by a fluorescence lifetime measuring instrument C11367 (Hamamatsu Photonics Trading Co., Ltd.).

Scanning electron microscopy. The morphology was observed using a Hitachi S-4800 scanning electron microscope (SEM) coupled with an energy dispersive X-ray (EDX) analyzer. Liquid samples were prepared by dropping the dilute solution (0.2 mM) onto a silicon wafer. Hydrogels for SEM experiments were was freeze-dried for morphology measurements. The freeze-dried hydrogel was brittle-fractured in liquid nitrogen.

Dynamic light scattering spectroscopy and Zeta potential. Average hydrodynamic diameter (D_h) and Zeta potential of polymer aggregates was determined using a dynamic light scattering (DLS) (Zetasizer Nano ZS, Malvern Instrument Ltd., UK) instrument. Each sample (0.2 mM) was filtered with a syringe filter prior to analysis.

Tensile tests. Mechanical tests were performed with dumbbell-shaped hydrogels specimens with a thickness of 1 mm standardized as DIN-53504 S3 (overall length: 35 mm; width: 6 mm; inner width: 2 mm, gauge length: 10 mm), using a commercial test machine (Electronic Testing Machine, RGM-6005, China) at a crosshead speed of 100% min^{-1}.

Rheological tests. Time sweeps were performed on a ARES-G2 rheometer (Waters) with plate-plate geometry (diameter of 25 mm, gap is 200 μm).The test was performed in the oscillation mode. Frequency and strain values were fixed to 1 Hz and 1%, respectively. Samples left 24 hours before being measured.

Sample-cutting. A laser cutting machine (GY-460 80W) was applied to cutting hydrogels or filter papers into various shapes.

pH Measurement. The pH values were measured by the PHSJ-3F pH meter (Shanghai REX, China).

Photography. Photographs were taken with a Canon digital camera.

Calculations

The geometries of the TPE3N and $TPE3N^{3+}$ at the ground state were fully optimized by means of the B3LYP/6-31G(d) level method. Density functional theory (DFT) calculations at the B3LYP/6-31G(d) level were performed in the Gaussian 09 package. These molecular orbitals were visualized using Gauss view 5.0.8 program. Distribution of different species of TPE3N and protonated TPE3N with different pH values were calculated using software of ChemAxon. RGD

surface was analyzed from the information of the calculation result and generated by Multiwfn 3.6. The double-exponential function used for fitting time-resolved fluorescence decay traces is given as: $I(t)=I_0+A_1\exp(-t/\tau_1)+A_2\exp(-t/\tau_2)$. The average fluorescence life time (τ) is calculated using the equation [1]: $\tau_{avg}=(A_1\tau_1^2+A_2\tau_2^2)/(A_1\tau_1+A_2\tau_2)$.

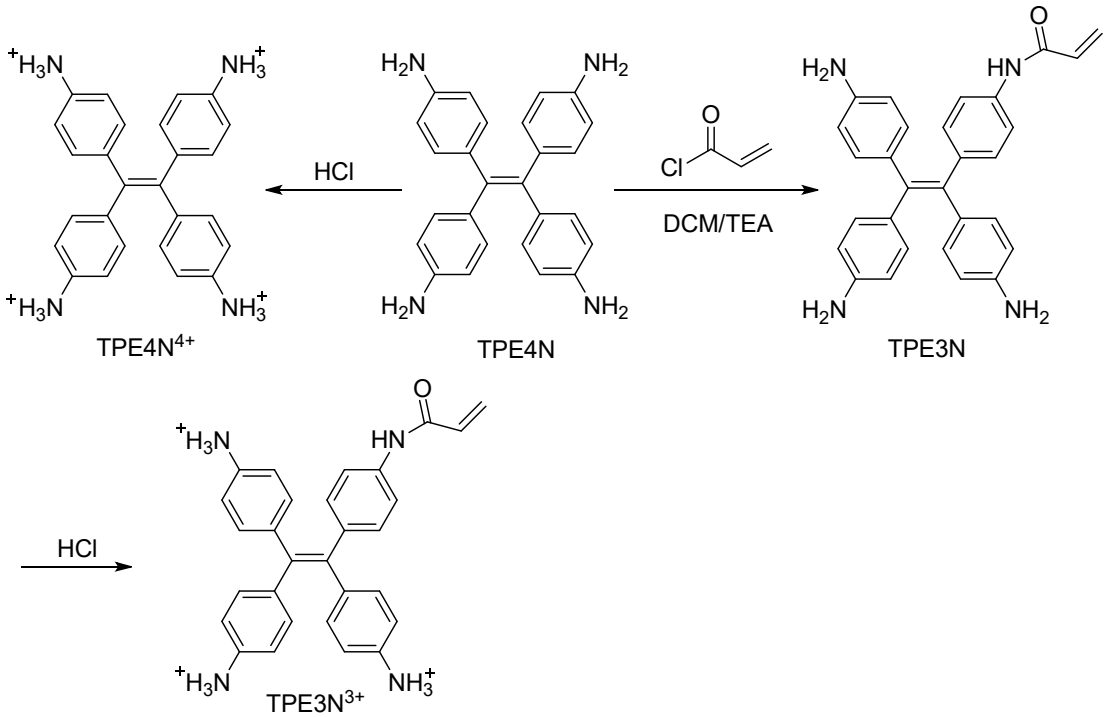

Figure S1 Synthetic scheme of TPE3N and $TPE3N^{3+}$

Synthesis of TPE4N and $TPE4N^{4+}$

TPE4N and $TPE4N^{4+}$were synthesized according to the reported method[2].

Synthesis and characterization of TPE3N

TPE4N (1 g, 2.55 mmol) were placed in a 250 mL round-bottom flask. Dichloromethane (200 mL) was added to the flask under nitrogen atmosphere. Then, 20 mL triethylamine (TEA) was added slowly. The reaction mixture was cooled to 0 °C and stirred for 30 min. Dichloromethane (100 ml) containing acryloyl chloride (207 μL, 2.55 mmol) were added dropwise to flask through a dropping funnel. The mixture was stirred for 72 h at room temperature. A gray precipitate was observed. The solid was collected by suction filtration and washed twice with dichloromethane, followed by drying under vacuum at 25 °C. TPE3N (gray solid, 0.76 g) was obtained with a yield of 67 %. ^{1}H NMR (400 MHz, DMSO-d_6) δ 10.25 (s, 1H), 7.47 (d, J=8.1 Hz, 2H), 6.96-6.82 (m, 2H), 6.57 (d, J=8.1 Hz, 6H), 6.43 (d, J=10.6 Hz, 1H), 6.32-6.19 (m, 7H), 5.72 (dd, J=10.6, 1.8 Hz, 1H), 5.05 – 4.71 (m, 6H).^{13}C NMR (101 MHz, DMSO-d_6) δ 163.58, 146.57, 139.09, 137.91,

133.36, 132.49, 132.15, 131.72, 126.96, 119.14, 113.61, 63.15, 52.51, 7.72. MS-ES$^+$(m/z) $C_{29}H_{26}N_4O$ Calculated 446.21; Found 447.2173.

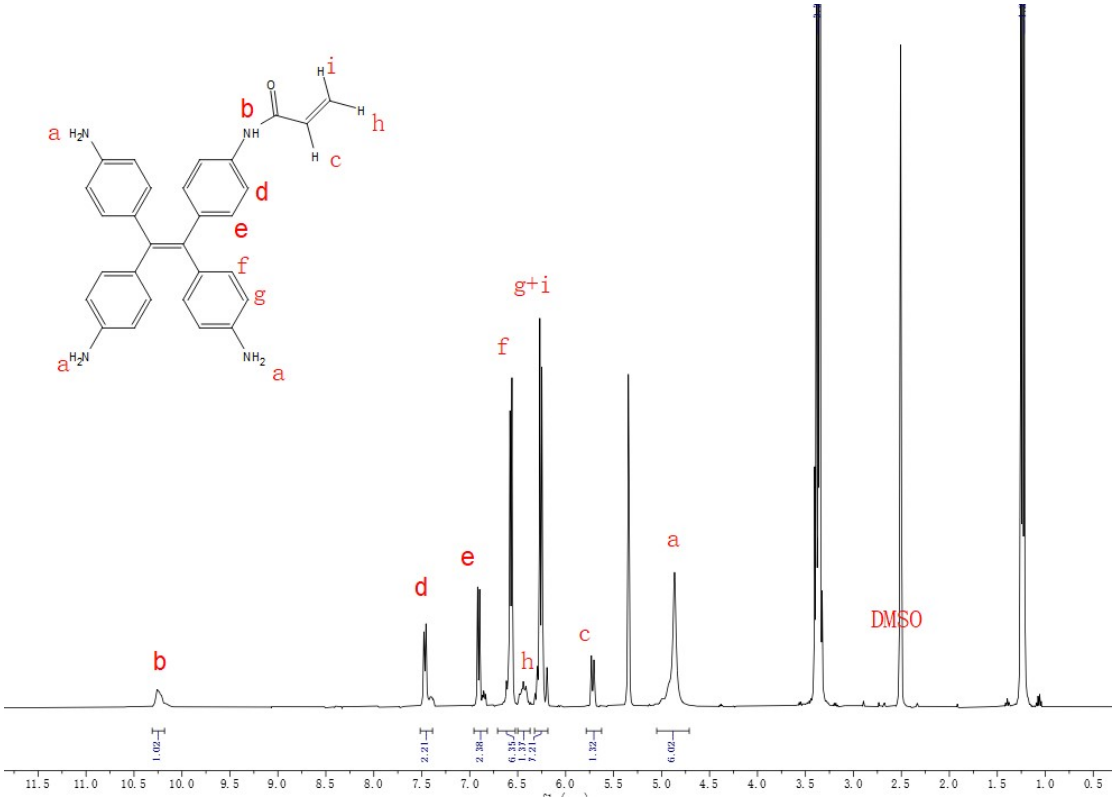

Figure S2 ^{1}H NMR of TPE3N

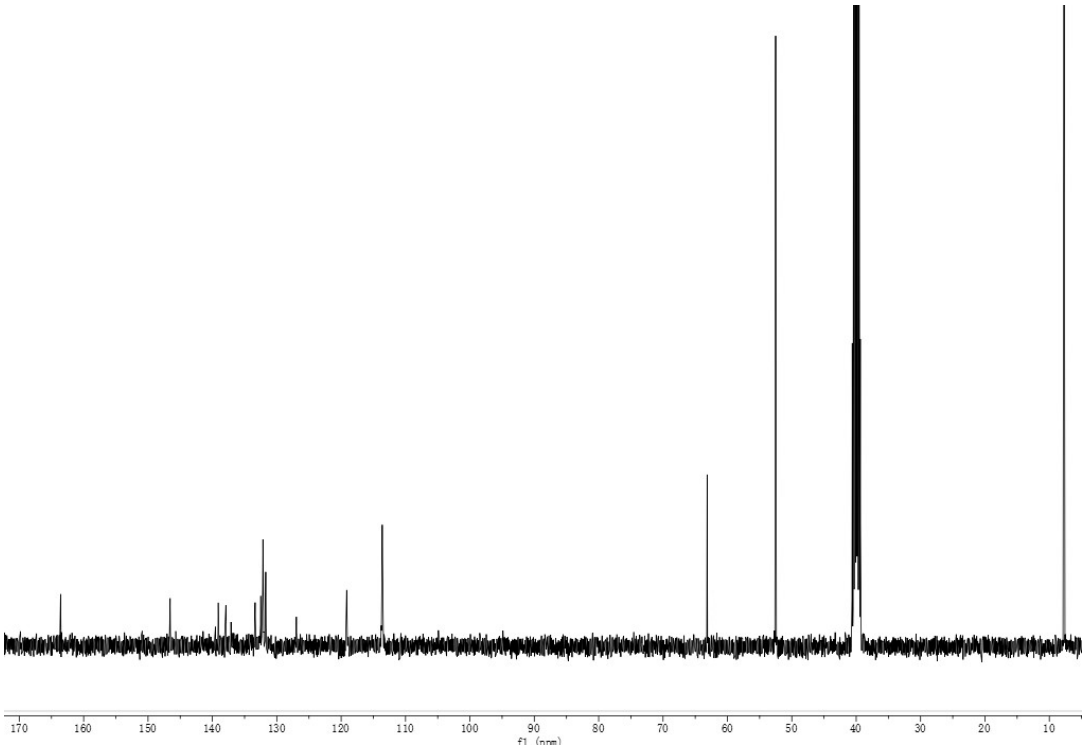

Figure S3 ^{13}C NMR of TPE3N

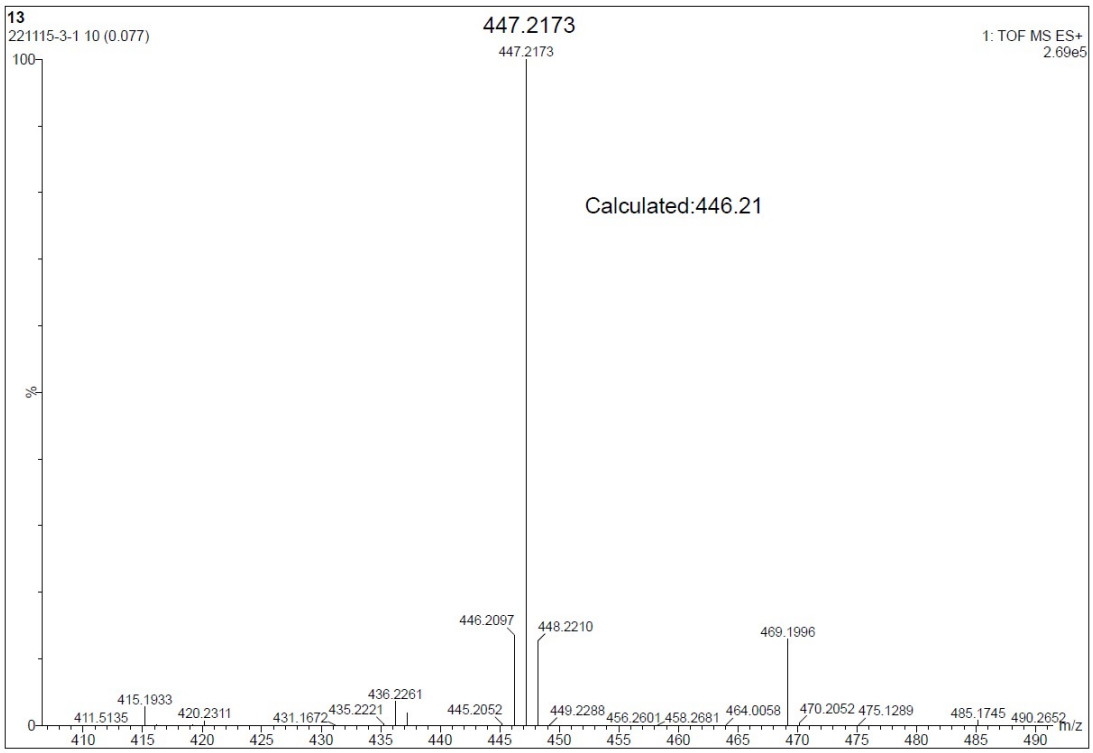

Figure S4 Mass spectrum of TPE3N

Synthesis of $TPE3N^{3+}$

TPE3N (0.894 g, 2 mmol) was dissolved in dilute hydrochloric acid and the solution was concentrated to obtain $TPE3N^{3+}$ (0.778 g, yield 70%) as a gray solid under reduced pressure.

Preparation of fluorescent hydrogel ($TPE3N^{3+}$-hydrogel)

DMA monomers (1.2 g), $TPE3N^{3+}$ monomers (40 mg), SN solution (4.2g), BIS (12 mg) and I2959 (12 mg) were dissolved in 6 mL of deionized water and stirred to obtain a homogenous solution. Then, the solution was transfused to a glass mold, including a layer of silica plate (1 mm) with a specific shape sandwiched between two glass plates (4 mm). The mold was sealed then irradiated under UV light (365 nm, 30 mW/cm^2) for 5 min. The SEM images showed that the dried $TPE3N^{3+}$-hydrogel exhibited porous structures.

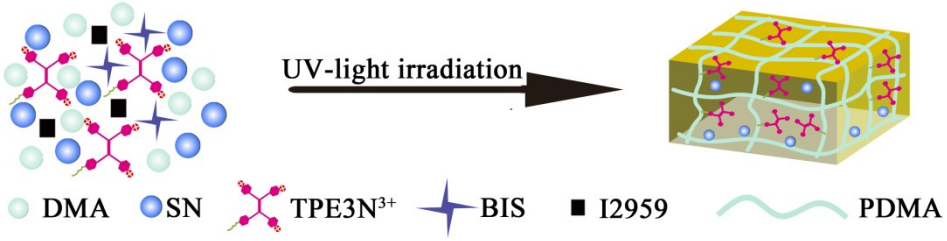

Figure S5 Schematic illustration of polymerization process of $TPE3N^{3+}$-hydrogel

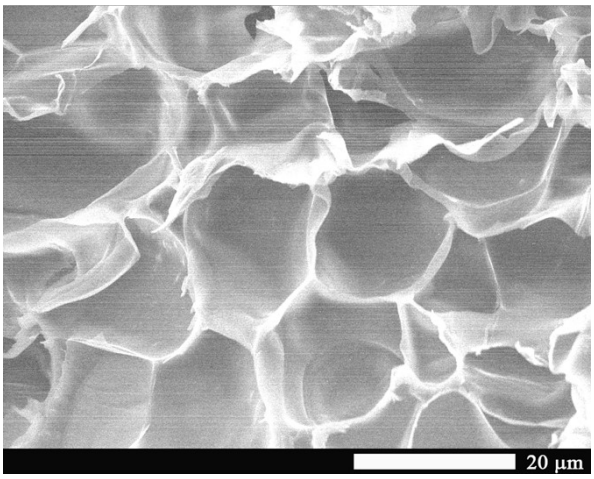

Figure S6 SEM image of $TPE3N^{3+}$-hydrogel

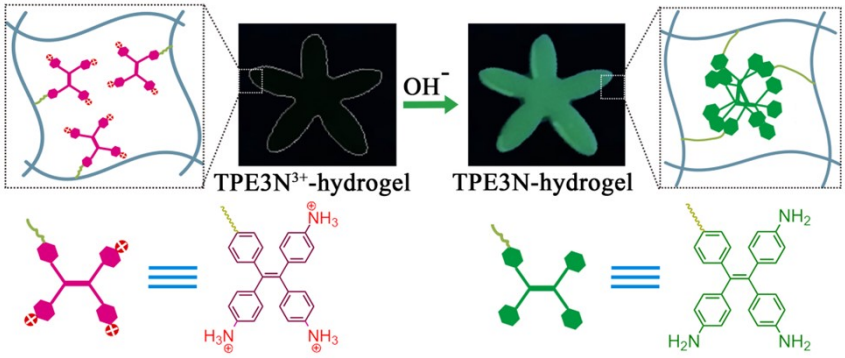

Figure S7 Images of $TPE3N^{3+}$-hydrogel and TPE3N-hydrogel under a 365 nm UV lamp and schematic illustration of the fluorescence mechanism

Determination of pKa value

The pH profile of TPE3N was determined by potentiometric acid-base titration. In 150 mM of NaCl aqueous solution (10 mL) saturated with nitrogen gas, 0.25 mmol TPE3N were dissolved. The pH of solution was set to 2 with 1 M HCl prior to titration. Subsequently, potentiometric titration was carried out with 0.1 M NaOH using an automatic titrator. The pKa value was obtained according to the plateau values of the titration curves. The plateau values indicated that the pKa value of TPE3N was 4.48.

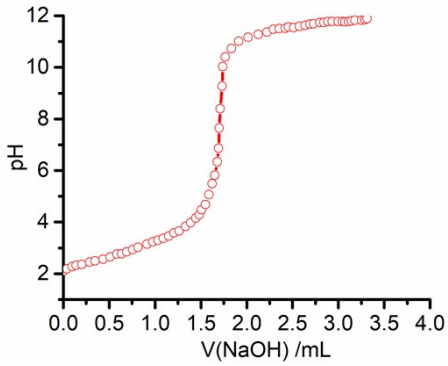

Figure S8 pH profiles of acid-base titration of TPE3N with 0.1 M NaOH.

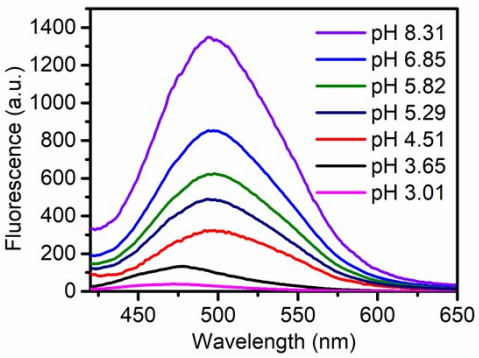

Figure S9 The pH-dependent fluorescence emission spectra of TPE3N^{3+}-hydrogel samples in different buffered solutions

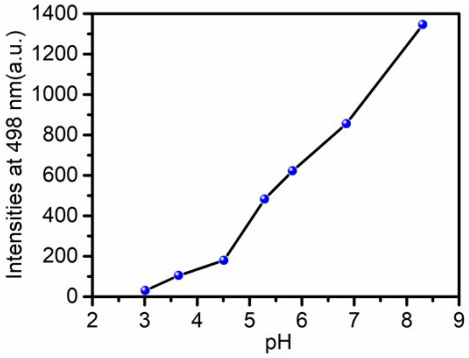

Figure S10 The peak fluorescence intensities of the TPE3N^{3+}-hydrogel samples at 498 nm in different buffered solutions

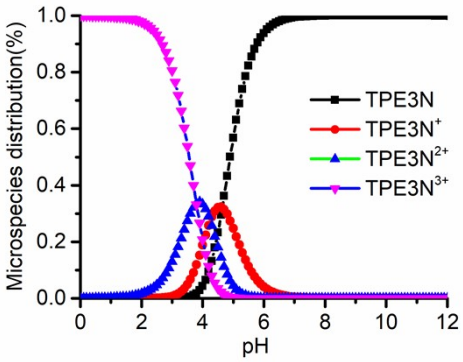

Figure S11 Distribution of different species of TPE3N and protonated TPE3N with different pH values calculated using ChemAxon

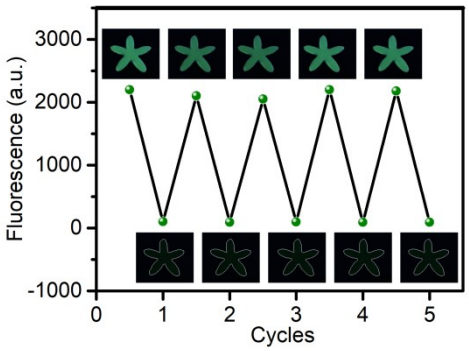

Figure S12 Fluorescence intensity change of the TPE3N^{3+}-hydrogel at 498 nm after being treated sequentially by NaOH and HCl solutions (0.1 M).

The pH-responsive mechanism of the TPE3N^{3+}-hydrogel

In order to investigate the pH-responsive mechanism of the TPE3N^{3+}-hydrogel, monomer TPE3N^{3+} was selected as a model compound. A series of TPE3N^{3+} solution with different pH values from 3.01 to 8.31 was employed for UV-Vis studies. The level-off tail observed in the UV spectrum in the longer wavelength region at pH 5.29 showed clear evidence of formation of

nanoscale aggregates[3]. The energy gap (ΔE) between HOMO and LUMO of $TPE3N^{3+}$ (1.9 eV) is more than that of TPE3N (1.48 eV). This result was consistent very well with the experiment that red-shift was observed in absorption spectra at high pH values. Dynamic laser scattering (DLS) examination revealed that average hydrodynamic diameter (D_h) of the nanoparticles increased with pH increase. The average D_h was 91 nm at pH 3.01, while D_h was 712 nm at pH 8.31. In addition, the scan electron microscopy (SEM) image displayed the formation of nanosized aggregates. The proton-binding behavior is proved by measuring the zeta potential. The positive zeta potential decreased from approximately +1.15 to +0.12 mV as the pH value increased from 3.01 to 8.31. The result might be attributed that the positively charged $TPE3N^{3+}$ was in a deprotonated state as pH increases.

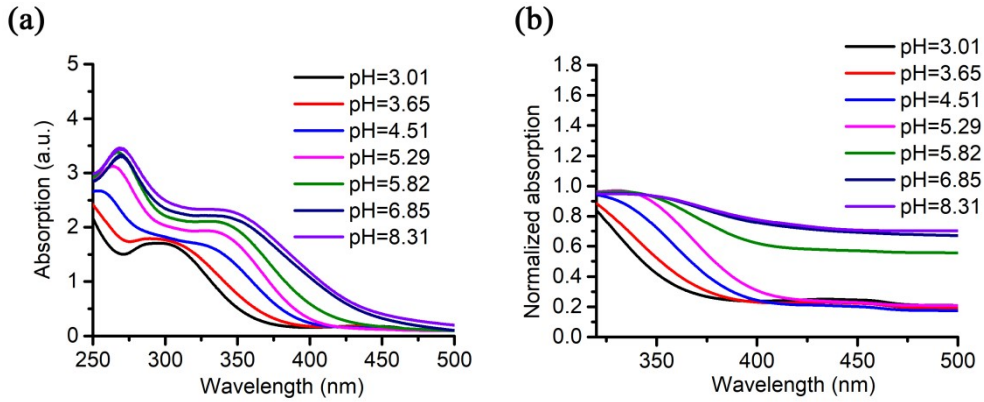

Figure S13 (a) UV-Vis and (b) Normalized UV-Vis absorbance spectra of $TPE3N^{3+}$ in different buffered solutions

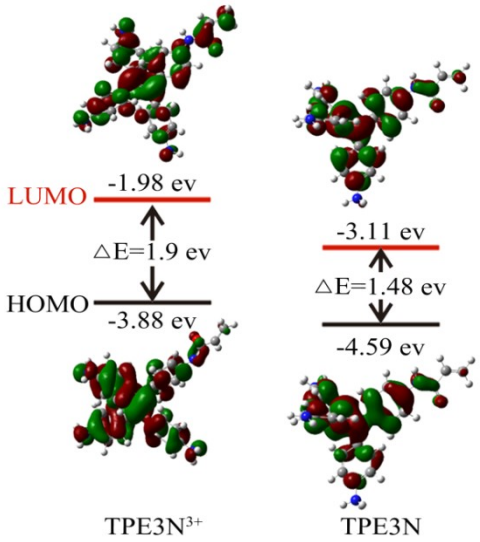

Figure S14 The energy of highest occupied molecular orbital (HOMO) and lowest unoccupied molecular orbital (LUMO) of $TPE3N^{3+}$ and TPE3N, respectively.

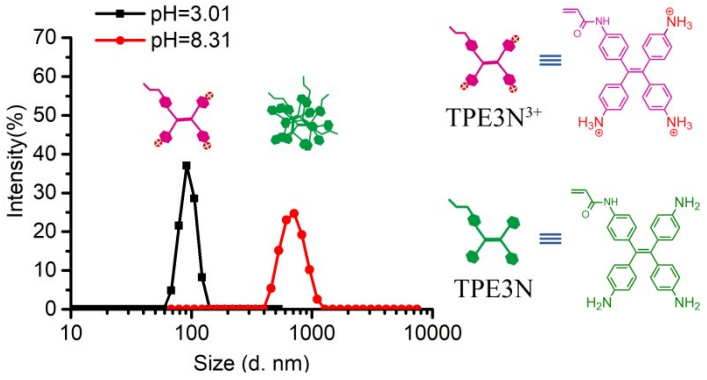

Figure S15 Hydrodynamic size distributions at pH 3.01 and 8.31 for $TPE3N^{3+}$

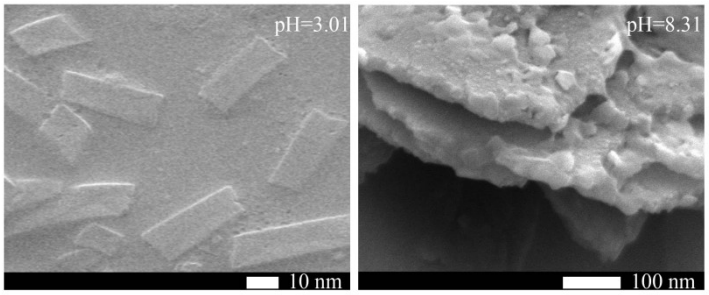

Figure S16 SEM images of $TPE3N^{3+}$ at pH 3.01 and 8.31

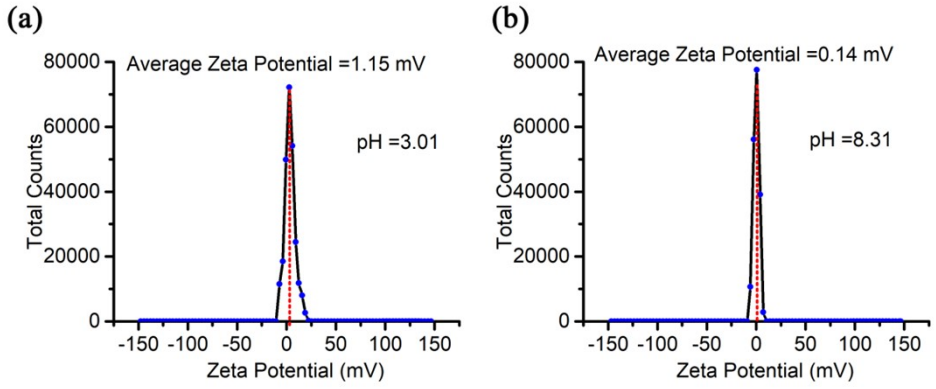

Figure S17 Zeta potential of $TPE3N^{3+}$ at pH 3.01 and 8.31

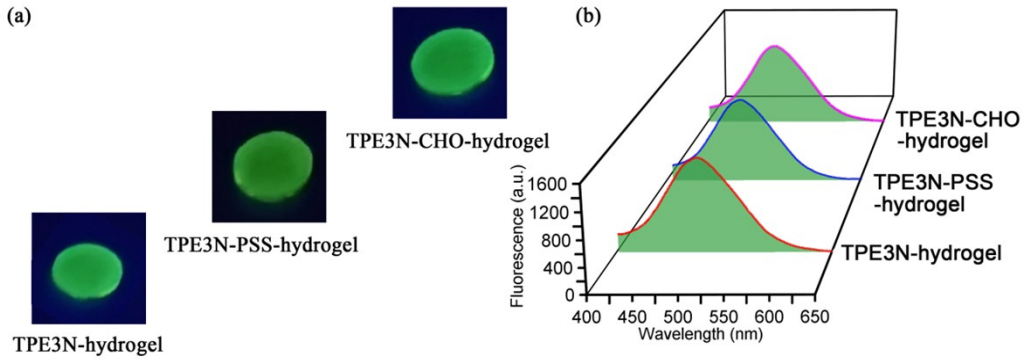

Figure S18 (a) Fluorescence images taken under a 365 nm UV lamp and (b) fluorescence emission spectra of TPE3N-hydrogel, TPE3N-PSS-hydrogel and TPE3N-CHO-hydrogel.

The mechanism of the fluorescence change of TPE3N-PSS-hydrogel and TPE3N-CHO-hydrogel

To partially verify the proposed mechanism above, the $TPE4N^{4+}$ (protonated TPE4N) was selected as a model compound to conduct the same reactions with PSS and alkaline HCHO, respectively. Increased fluorescence and particle size revealed that the electrostatic interactions or dynamic imine bonds of the initially dispersed molecule $TPE4N^{4+}$ with the PSS or HCHO could undergo aggregate formation (named TPE4N-PSS and TPE4N-CHO aggregate). For further demonstration of the electrostatic interactions between $TPE3N^{3+}$-gel and PSS, RDG analysis was used. $TPE4N^{4+}$ and *p*-Toluenesulfonate were used as model compounds. Optimized structures of $TPE4N^{4+}$ and *p*-toluenesulfonate were shown in Figure 2c. It can be seen that electrostatic interactions form between protonated amino groups and *p*-toluenesulfonate, and strong interactions appeared among four benzene units in the center of $TPE4N^{4+}$ restrict the molecular rotation of the benzene units.[4-6]

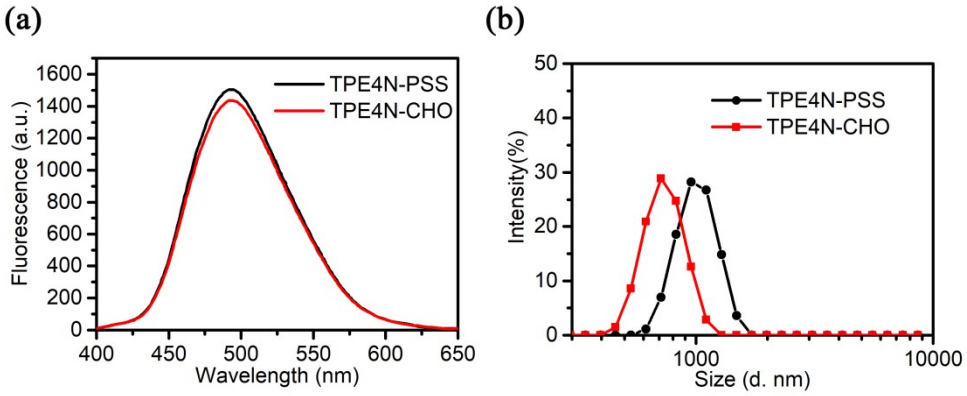

Figure S19 (a) Fluorescence emission spectra and (b) hydrodynamic size distributions of TPE4N-PSS and TPE4N-CHO aggregates

The pH-responsiveness of the $TPE4N^{4+}/OH^-$, $TPE4N^{4+}$/PSS, and $TPE4N^{4+}$/CHO aggregate system

Based on the deprotonation of the amino groups of $TPE4N^{4+}$, electrostatic interactions or dynamic imine bonds，three kinds of model aggregates were first prepared from the $TPE4N^{4+}$ solutions, mixture of $TPE4N^{4+}$ and PSS, mixture of $TPE4N^{4+}$ and HCHO solution at pH 8.31.The three model aggregate systems are labeled as $TPE4N^{4+}/OH^-$, $TPE4N^{4+}$/PSS and $TPE4N^{4+}$/CHO aggregate, respectively. In the next step, the pH was decreased slowly by adding small quantities of adequately diluted HCl solutions, keeping in mind that the total volume of the solution does not change any appreciably. Changes in the AIE behavior for $TPE4N^{4+}/OH^-$, $TPE4N^{4+}$/PSS and

$TPE4N^{4+}$/CHO aggregate were investigated as a function of the changing pH of the solution and the results are shown in Figure S20a. All of the model aggregate systems clearly show a pH-dependent emission decay with only minimal differences. Next, we discuss the causes of the variation in fluorescence intensity in detail. As shown in Figure S20b, for $TPE4N^{4+}/OH^-$ aggregate system, fluorescence intensity decreases very sharply around pH 4.51 due to the pKa value of TPE4N being approximately 4.6[2]. Hydrophilic $TPE4N^{4+}$ forms can deprotonate to TPE4N with hydrophobicity, forming TPE4N aggregates during the pH region above 4.6. While pH decreased to less than 4.51(below pKa of TPE4N), the neutral TPE4N was in a protonated state and positively charged, existing as $TPE4N^{4+}$ form. The electrostatic repulsion of molecules will become dominant and prevent molecules from aggregation, corresponding to the almost non-emission of the solution. For $TPE4N^{4+}$/PSS aggregate system (Figure S20c), in the pH region of 5.29-8.31, aggregate exists in the TPE4N aggregate form similar to $TPE4N^{4+}$ aggregate system. When the pH decreases from 4.51 to 3.65, fluorescence intensity increases followed by a sharp decline and reaches equilibrium with pH below 3.65. The reason for fluorescence increase is reformed TPE4N-PSS aggregates via the stronger electrostatic interactions between $TPE4N^{4+}$ and PSS. However, the sharp decrease fluorescence intensity at pH 3.01 cannot be attributed to any protonation process for the PSS, because the pKa values for the sulfonic acid groups of the PSS are largely negative [7,8]. Therefore, we feel that, at this lower pH region, the changing ionic strength of the solution is mainly responsible for the changing fluorescence. This is expected because the increasing ionic strength would cause a screening effect for the electrostatic interaction of the $TPE4N^{4+}$ with the PSS, resulting the disintegration of the TPE4N-PSS aggregates present in the solution[9]. To support this proposition, we performed emission studies for the $TPE4N^{4+}$/PSS aggregate system in the presence of gradually increasing concentration of NaCl, and the results are shown in Figure S21. It indicates that, with increasing salt concentration, the fluorescence intensity of the initially formed TPE4N-PSS aggregates decreases very sharply, suggesting the salt induced disintegration of the TPE4N-PSS aggregates. For $TPE4N^{4+}$/HCHO aggregate system (Figure S20d), at high pH values the ammonium ions in $TPE4N^{4+}$ are deprotonated to $-NH_2$ and can react with HCHO to form imines (Schiff bases)[10], leading to formation of TPE4N-CHO aggregates accompanied with enhanced fluorescence. When pH is lowered to ~5.4, imine bonds break gradually and decompose into TPE4N and HCHO. At this

moment, it shows little effect on fluorescence intensity due to formed TPE4N aggregates. But, when pH drops further below the pKa of TPE4N, $TPE4N^{4+}$ appears, fluorescence intensity decreases rapidly. Therefore, for $TPE4N^{4+}$/CHO aggregate system, the change of fluorescence intensity was ascribed to subsequent appearance of TPE4N-CHO aggregates, TPE4N aggregates and $TPE4N^{4+}$ as the pH drops.

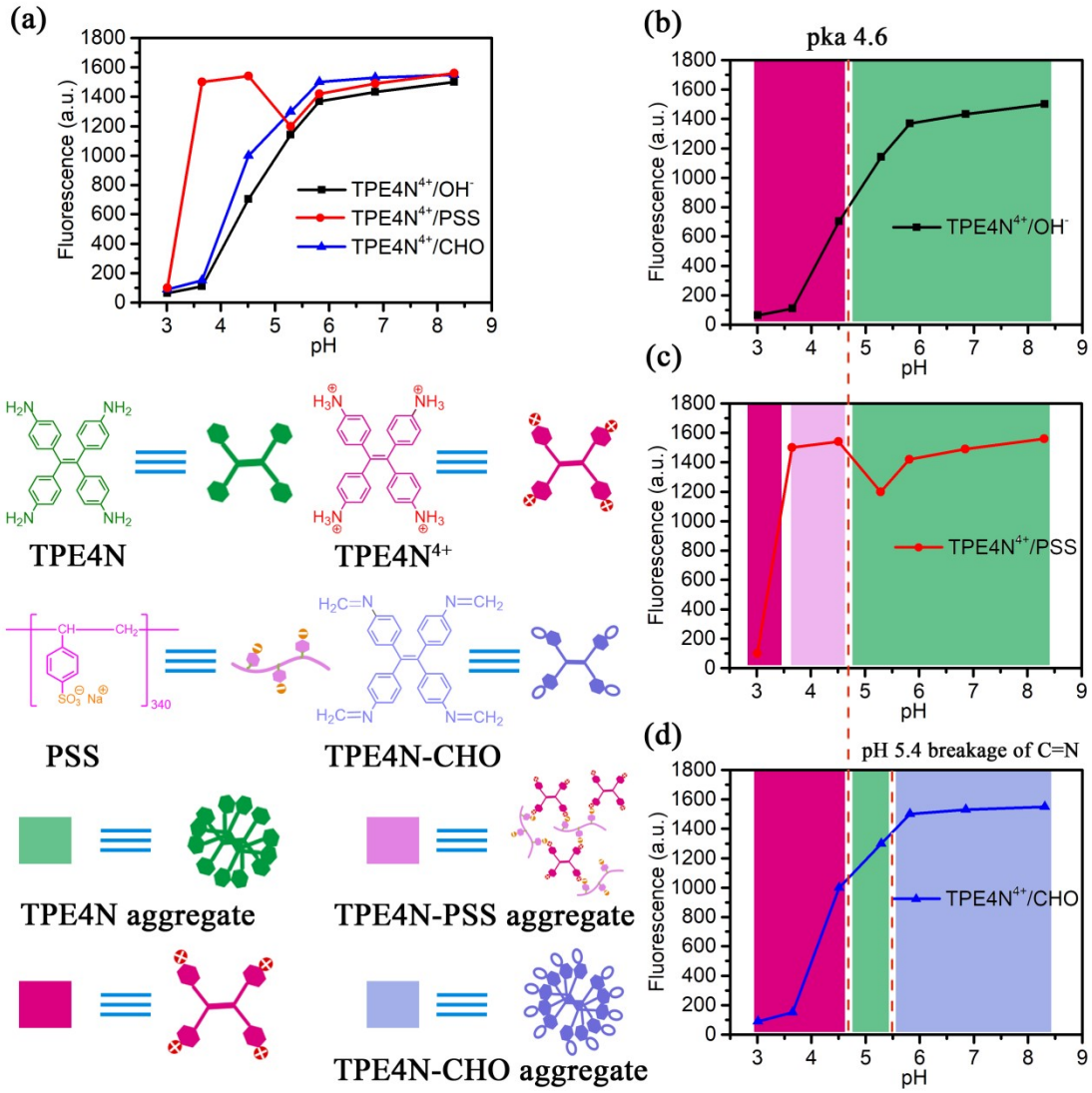

Figure S20 Fluorescence intensity changes of $TPE4N^{4+}/OH^-$, $TPE4N^{4+}$/PSS and $TPE4N^{4+}$/CHO aggregate systems as a function of pH.

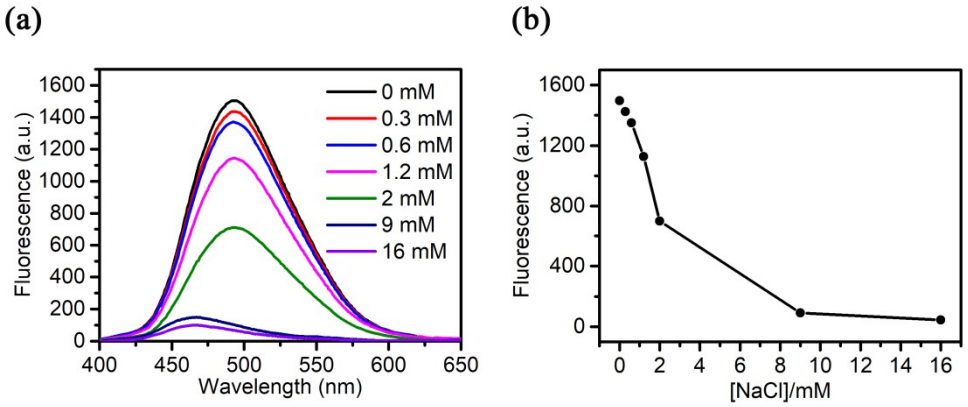

Figure S21 (a) Emission spectra of TPE4N-PSS aggregate system at pH 3.65 with increasing NaCl concentration. (b) Fluorescence intensity changes at 498 nm with increasing NaCl concentration.

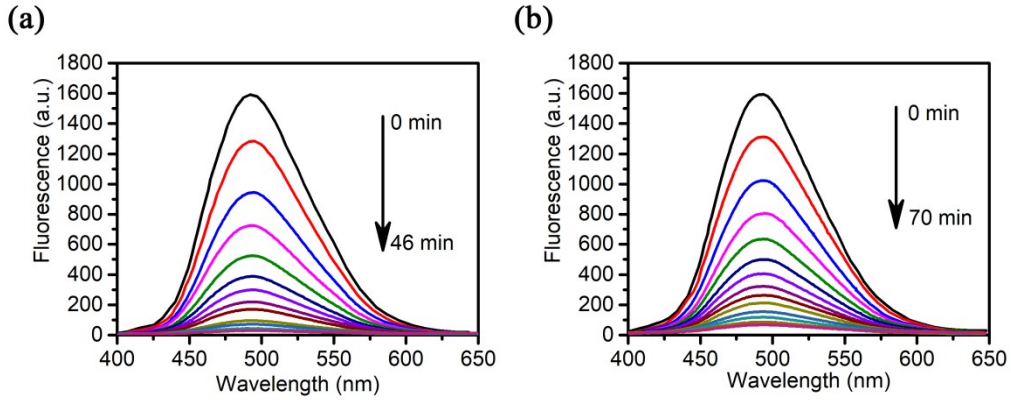

Figure S22 The gradual change in the emission spectra of (a) $TPE4N^{4+}$/PSS and (b) $TPE4N^{4+}$/CHO aggregate system in pH 3.01 solution with the prolongation of time.

Fluorescence Lifetime Measurements of the TPE3N-hydrogel, TPE3N-PSS-hydrogel and TPE3N-CHO-hydrogel

The fluorescence lifetimes were determined from the fluorescence decay curves. Generally, the lifetime is influenced by the environment of the AIE luminogen; a prolonged fluorescence lifetime reflects a more immobilized state and stronger interactions surrounding the AIE luminogen.[13-15] Figure S23 displays the decay curves of TPE3N-hydrogel, TPE3N-PSS-hydrogel and TPE3N-CHO-hydrogel. Being fitted by a double exponential function, their average fluorescence lifetimes (τ) were calculated to 2.48 ns, 7.72 ns and 10.54 ns, respectively.

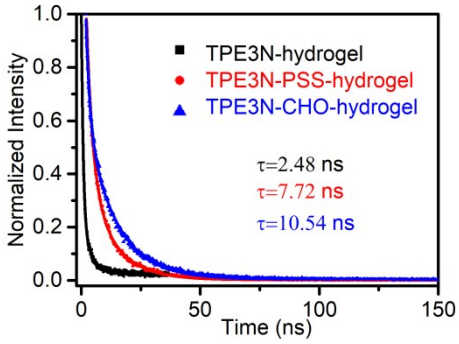

Figure S23 The fluorescence decay curves of TPE3N-hydrogel, TPE3N-PSS-hydrogel and TPE3N-CHO-hydrogel

Preparation of the PAA-hydrogel

The PAA-hydrogel was also prepared by radical polymerization. Predetermined amounts of DMA (3.0 g), AA (3.0 g) and BIS (0.008 g) were dissolved in H_2O (15 ml). The solution was purged with nitrogen for 15 min to remove oxygen, and then AIBN (0.02 g) was added. The aqueous reaction mixture was injected into a mold with space of 100 × 50 × 1 mm^3, which was formed by a transparent glass plate and a polytetrafluoroethylene (PTFE) spacer with thickness of 1 mm. Next, gelation was carried out in an oven at 65 ^oC for 10 h. The mould was then removed from the oven, and the bulk hydrogel obtained from the mould was soaked in water for hours, then repeatedly washing with water to remove unreacted monomers and initiators. Subsequently, the hydrogels were cut into different shapes with a laser cutting machine.

Time sweep rheology of the $TPE3N^{3+}$ and PAA-hydrogel

To determine values of storage modulus(G') and loss modulus(G"), time-sweep oscillatory rheology was performed on $TPE3N^{3+}$-hydrogel and PAA-hydrogel at different pH values. Figure S24 shows that G' for both $TPE3N^{3+}$-hydrogel and PAA-hydrogel are higher than their respective G" and there is no obvious change in G' with time, suggesting that both $TPE3N^{3+}$-hydrogel and PAA-hydrogel exhibit viscoelasticity and they are structurally stable over the working time and pH range.

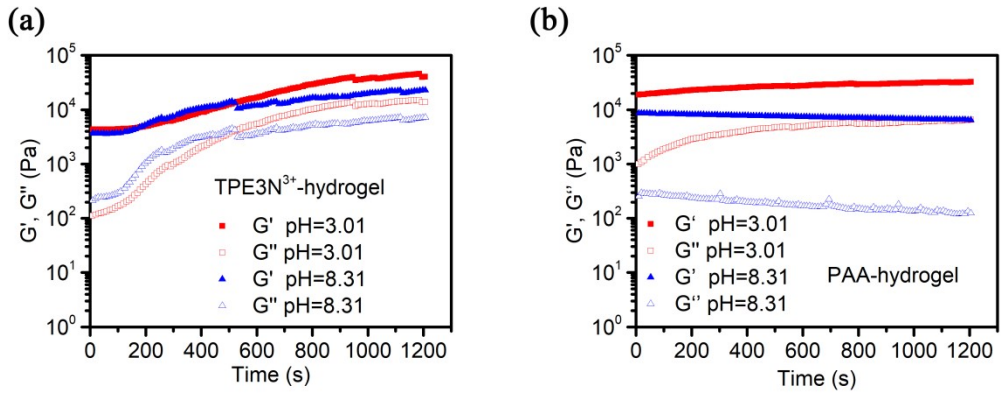

Figure S24 Variation of G' and G'' with time for TPE3N^{3+}-hydrogel and PAA-hydrogel at different pH values.

The fabrication and characterization of TPE3N^{3+}-hydrogel/PAA-hydrogel bilayer hydrogel

Based on specific interactions between N,N-dimethylacrylamide polymeric side-chains (PDMA) and SN[11,12], the bilayer hydrogel sheets were prepared by the interfacial adhesion between TPE3N^{3+}-hydrogel sheet and PAA-hydrogel sheets. The strip-shaped, hand-shaped and flower-shaped bilayer hydrogels were tailored from bilayer hydrogel sheet by a laser cutting machine (Figure S25). Scanning electron microscopy (SEM) images of the TPE3N^{3+}-hydrogel/PAA-hydrogel bilayer hydrogels show the typical and expected bilayer structure based on interfacial adhesion, which is linked by specific interactions between PDMA chains in the PAA-hydrogel network and inorganic SN in the TPE3N^{3+}-hydrogel network (Figure S26). Tensile stress-strain curves of the PAA-hydrogel, TPE3N^{3+}-hydrogel and PAA-hydrogel/TPE3N^{3+}-hydrogel overlapped at the ends with a contact area of about 100 mm^2 was also measured. The adhesion between the PAA-hydrogel/TPE3N^{3+}-hydrogel strips was measured to be very strong and hardly separated. The fractured stress strengths and fractured strains can satisfy shape deformation completely.

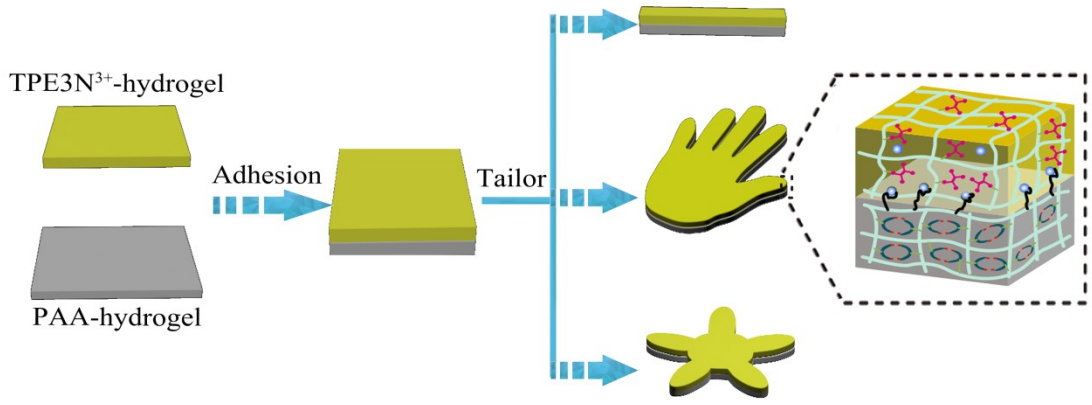

Figure S25 Schematic illustration of the fabrication process of the bilayer hydrogels with different shapes

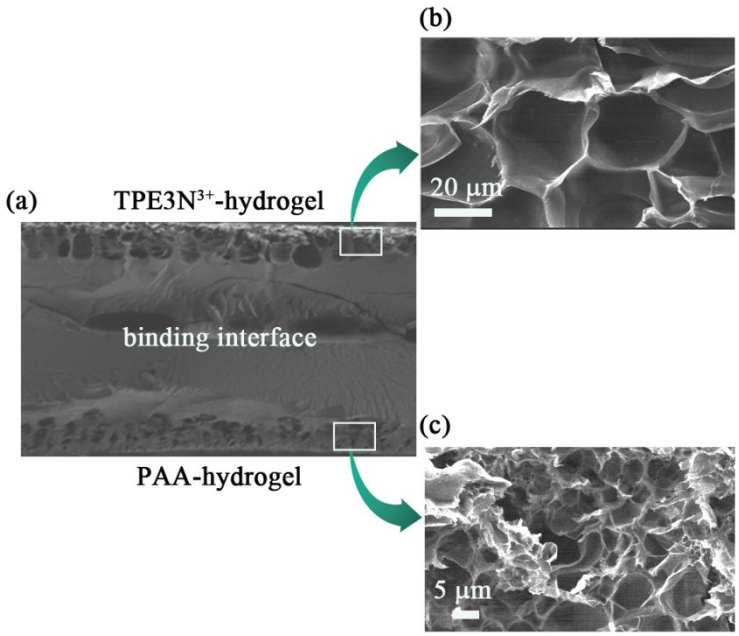

Figure S26 (a) Cross-section SEM image of the interface of freeze-dried $TPE3N^{3+}$-hydrogel/PAA-hydrogel bilayer hydrogel strip. (b) SEM image of the freezed-dried $TPE3N^{3+}$-hydrogel layer. (c) SEM image of the freeze-dried PAA-hydrogel layer.

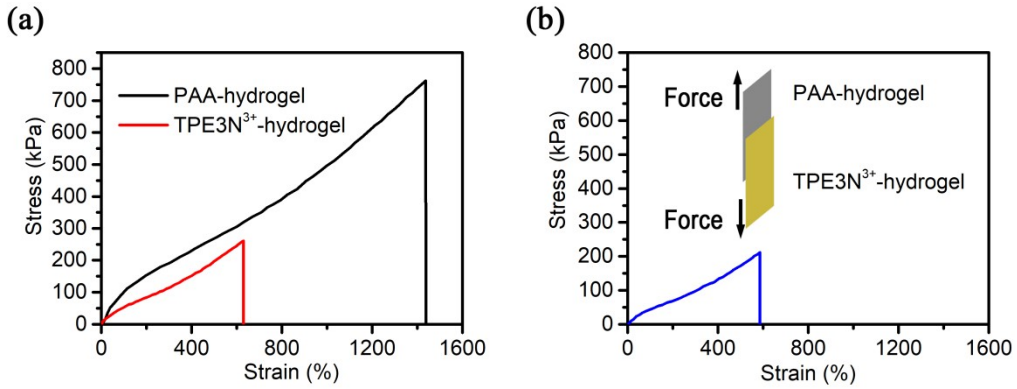

Figure S27 (a) Tensile stress-strain curves of the PAA-hydrogel and $TPE3N^{3+}$-hydrogel. (b) The stress-strain curves of PAA-hydrogel/$TPE3N^{3+}$-hydrogel overlapped at the ends with a contact area.

The SDFC behavior of the $TPE3N^{3+}$-hydrogel/PAA-hydrogel bilayer hydrogel

The deformation behavior in response to pH change was primarily caused by the large mismatch of swelling capability between the $TPE3N^{3+}$-hydrogel and PAA-hydrogel layers. Their equilibrium swelling ratio (ESR) upon variation of pH value was investigated (Figure S28). The ESR of the PAA-hydrogel increases from approximately 9 to 30 as the pH value rises from 3 to 12, with a dramatic change occurring between pH values of 4 and 6 due to the pKa value of AA being approximately 4.25. For the $TPE3N^{3+}$-hydrogel, the ESR remains constant regardless of the pH

values. The different ESRs may result in asymmetrical deformation of the TPE3N^{3+}-hydrogel/PAA-hydrogel bilayer hydrogel with reversible bending under different pH conditions.

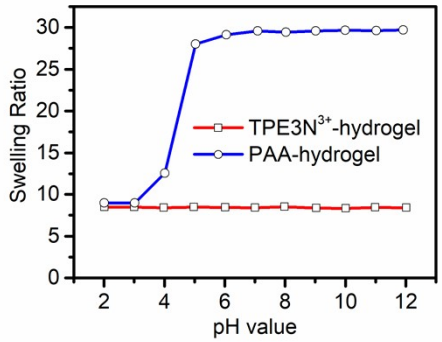

Figure S28 Equilibrium swelling ratio of the TPE3N^{3+}-hydrogel and PAA-hydrogel upon variation of pH value.

Next we investigated effect of thickness of the layers on the bending. Based on the obtained ESR, the bending of TPE3N^{3+}-hydrogel/PAA-hydrogel bilayer hydrogel mainly depends on PAA-hydrogel bilayer. Therefore, the thickness of the TPE3N^{3+}-hydrogel layer was fixed to 1 mm whereas the thickness of PAA-hydrogel layer was varied (0.5, 0.8, 1, 1.5 and 2 mm). As shown in Figure S29b, notably, the bending degree increases with the thickness of the hydrogel layer from 0.5 to 1 mm at 25 °C (from 200° to 330°). This result proves that a thicker hydrogel layer produces a greater driving force over a definite thickness range.[16,17] However, a further increase in the hydrogel thickness from 1 to 2 mm results in a decrease in the bending degree from 330° to 290° at 25 °C. It is because the bending degree is mainly controlled by the actuation strain and the hydrogel layer thickness.[18] As demonstrated above, the PAA-hydrogel with a thickness of 1 mm illustrated the largest bending degree which suggests that the optimum thickness for the PAA-hydrogel is then around 1 mm. the PAA-hydrogel and TPE3N^{3+}-hydrogel with a thickness of 1 mm was thus used in the following experiments. SDFC change of the TPE3N^{3+}-hydrogel/PAA-hydrogel bilayer hydrogel strip were observed when the solution pH was alternately varied between 3.01 and 8.31. In addition, the pH-triggered SDFC behavior owns excellent multicycle reversibility, which is important for the application of repeated information encryption/decryption.

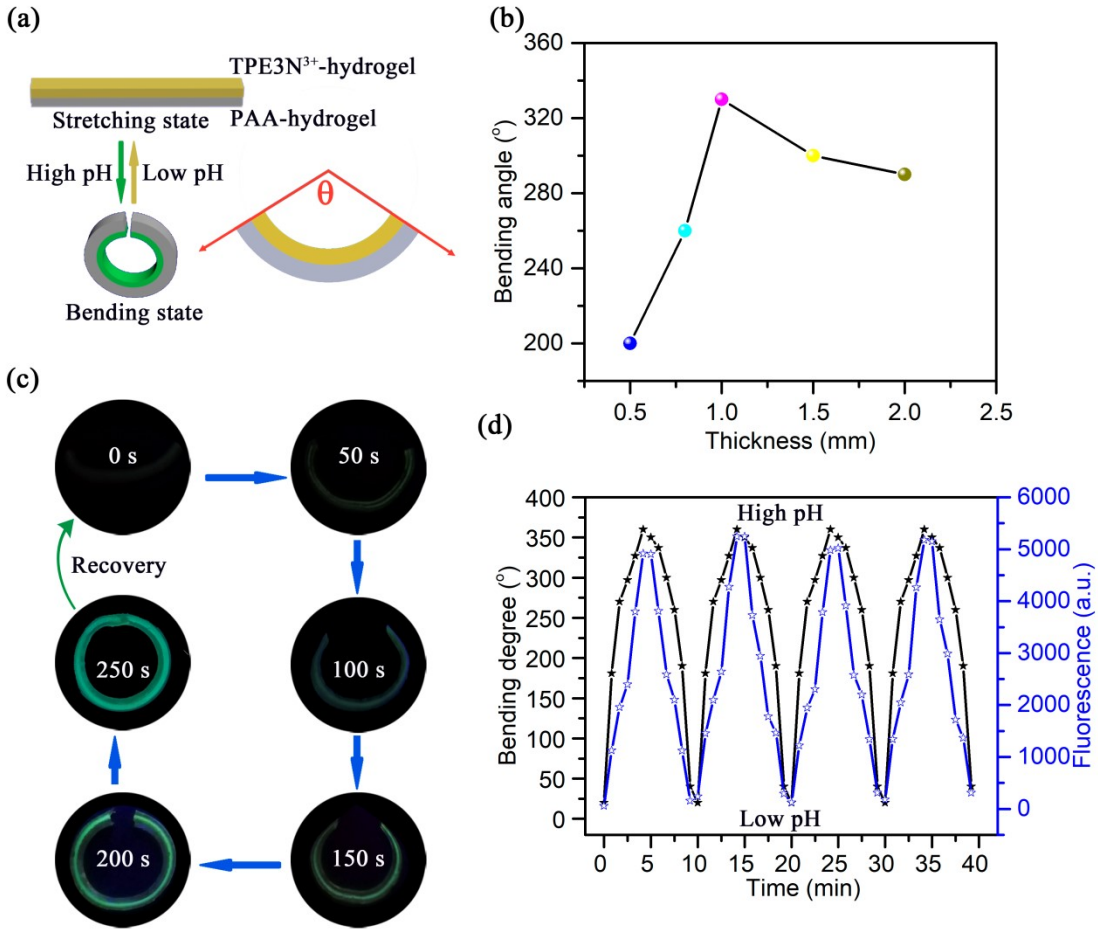

Figure S29 (a) Schematic representation of SDFC behavior. (b) Effects of the thickness on the bending behaviors of bilayer hydrogel. (c) Photographs of the SDFC behavior of the TPE3N^{3+}-hydrogel/PAA-hydrogel bilayer hydrogel strips after soaked in pH 9 and 3 buffer solution at different time under 365 nm UV light, respectively. (d) Cyclic SDFC behavior of the TPE3N^{3+}-hydrogel/PAA-hydrogel bilayer hydrogel. The θ is a central angle formed at the center of a circle by two radii.

References

[1] J.R. Lakowicz, Principles of Fluorescence Spectroscopy, Plenum Press, New York, 2006, https://doi.org/10.1007/978-0-387-46312-4.

[2] E. Liang, F. Su, Y. Liang, G. Wang, W. Xu, S. Li, C. Yang, J. Tang, N. Zhou, *Chem. Commun.* **2020**, 56, 15169.

[3] R. Hu, E. Lager, A. Aguilar-Aguilar, J. Liu, J. W. Y. Lam, H. H. Y. Sung, I. D. Williams, Y. Zhong, K. S. Wong, E. Peña-Cabrera, B. Z. Tang, *J. Phys. Chem. C* **2009**, 113, 15845.

[4] E. R. Johnson, S. Keinan, P. Mori-Sánchez, J. Contreras-García, A. J. Cohen, W. Yang, *J. Am. Chem. Soc.* **2010**, 132, 6498.

[5] T. Lu, F. Chen, *J. Comput. Chem.* **2012**, 33, 580.

[6] T. Lu, F. Chen, *J. Mol. Graphics Modell.* **2012**, 38, 314.

[7] J. P. Guthrie, *Can. J. Chem.* **1978**, 56, 2342.

[8] Serjeant, E. P.; Dempsey, B. (International Union of Pure and Applied Chemistry; Commission on Electrochemical Data). Ionisation Constants of Organic Acids in Aqueous Solution; IUPAC

Chemical Data Series, No. 23; Pergamon Press: Oxford, New York, 1979.
[9] G. Chakraborty, J. N. Malegaonkar, S. V. Bhosale, P. K. Singh, H. Pal, *J. Phys. Chem. B* **2021**, 125, 11122.
[10] I. Janica, V. Patroniak, P. Samorì, A. Ciesielski, *Chem. Asian. J.* **2018**, 13, 465.
[11] C. Yang, F. Su, Y. Xu, Y. Ma, L. Tang, N. Zhou, E. Liang, G. Wang; J. Tang, *ACS Macro Lett.* **2022,** *11*, 347.
[12] Rose, S.; Prevoteau, A.; Elzière, P.; Hourdet, D.; Marcellan, A.; Leibler, L. Nanoparticle solutions as adhesives for gels and biological tissues.*Nature* **2013**, 505, 382.
[13] S. J. Chen, Y. N. Hong, Y. Zeng, Q. Q. Sun, Y. Liu, E. G. Zhao, G. X. Bai, J. N. Qu, J. H. Hao and B. Z. Tang, *Chem.-Eur. J.*, **2015**, 21, 4315.
[14] M. X. Gao, Y. N. Hong, B. Chen, Y. N. Wang, W. J. Zhou, W. W. H. Wong, J. Zhou, T. A. Smith, Z. J. Zhao, *Polym. Chem.* **2017**, 8, 3862–3866.
[15] L. Espinar-Barranco, M. Meazza, A. Linares-Perez, R. Rios, J. M. Paredes, L. Crovetto, *Sensors* **2019**, 19, 4932.
[16] A. W. Hauser, A. A. Evans, J.-H. Na, R. C. Hayward, *Angew. Chem., Int. Ed*. **2015**, 54, 5434.
[17] X. Jin, Y. L. Hsieh, *Polymer* **2005**, 46, 5149.
[18] L. Ionov, *Adv. Funct. Mater*. **2013**, 23, 4555.